Three-dimensional electronic structure in ferromagnetic Fe3Sn2 with breathing kagome bilayers

Rapid Communications

Three-dimensional electronic structure in ferromagnetic Fe_3Sn_2 with breathing kagome bilayers

Hiroaki Tanaka,[1] Yuita Fujisawa,[2] Kenta Kuroda,[1,*] Ryo Noguchi,[1] Shunsuke Sakuragi,[1] Cédric Bareille,[1] Barnaby Smith,[2] Cephise Cacho,[3] Sung Won Jung,[3] Takayuki Muro,[4] Yoshinori Okada,[2] and Takeshi Kondo[1,5,†]

[1]*ISSP, University of Tokyo, Kashiwa, Chiba 277-8581, Japan*

[2]*Okinawa Institute of Science and Technology Graduate University, Okinawa 904-0495, Japan*

[3]*Diamond Light Source, Harwell Campus, Didcot OX11 0DE, United Kingdom*

[4]*Japan Synchrotron Radiation Research Institute (JASRI), 1-1-1 Kouto, Sayo, Hyogo 679-5198, Japan*

[5]*Trans-scale Quantum Science Institute, University of Tokyo, Bunkyo-ku, Tokyo 113-0033, Japan*

(Received 23 January 2020; accepted 27 March 2020; published 24 April 2020)

A large anomalous Hall effect (AHE) has been observed in ferromagnetic Fe_3Sn_2 with breathing kagome bilayers. To understand the underlying mechanism for this, we investigate the electronic structure of Fe_3Sn_2 by angle-resolved photoemission spectroscopy (ARPES). In particular, we use both vacuum ultraviolet light (VUV) and soft x ray (SX), which allow surface-sensitive and relatively bulk-sensitive measurements, respectively, and distinguish bulk states from surface states, which should be unlikely related to the AHE. While VUV-ARPES observes two-dimensional bands mostly due to surface states, SX-ARPES reveals three-dimensional band dispersions with a periodicity of the rhombohedral unit cell in the bulk. Our data show a good consistency with a theoretical calculation based on density functional theory, suggesting a possibility that Fe_3Sn_2 is a magnetic Weyl semimetal.

DOI: 10.1103/PhysRevB.101.161114

The translational symmetry of a crystal allows its eigenstates to be labeled by Bloch wave vectors in a reciprocal space [1], and the Berry curvature [2] defined there could cause several anomalous physical behaviors. The integration of the Berry curvature over the occupied states leads to an intrinsic anomalous Hall effect (AHE), which becomes nonzero under broken time-reversal symmetry. Moreover, in a two-dimensional system, the integration over the Brillouin zone (BZ) for each different band is quantized to an integer [3], which is called the Chern number and has attracted growing interests as a topological invariant [4]. Nonzero Chern number is realized, for example, in the honeycomb lattice model with gapped Dirac fermionic states [5]. An extension of these two-dimensional states to a three-dimensional crystal, under the breaking of time-reversal or space-inversion symmetry, which resolves spin degeneracy, is a Weyl semimetal [6], which has been intensively studied theoretically [7–10] and experimentally [11–16].

Graphene with Dirac fermionic states yielded by the honeycomb lattice [17] is known as a model case in which topological phenomena are well described. As another possible system hosting Dirac fermionic states, the two-dimensional ideal kagome lattice [Fig. 1(a)] has been proposed [18]. From this perspective, ferromagnetic Fe_3Sn_2 with the kagome lattice has been of recent interest in condensed matter physics. This compound is actually not composed of the ideal kagome lattice, but of the breathing kagome lattice [Fig. 1(b)], which is formed by upward and downward triangles with different sizes and therefore has two atomic bond lengths. Despite it, Fe_3Sn_2 exhibits various attractive properties, such as a large AHE [19,20], a topological Hall effect [21], large tunability of magnetization [22], gapped (massive) Dirac states [20], and flat bands near the Fermi energy [23]. Fe_3Sn_2 has been, therefore, expected to provide a new platform to study topological physics in the kagome network with broken time-reversal symmetry.

Previously, the origin of the AHE in Fe_3Sn_2 was proposed to be two-dimensional Dirac fermionic states with band gaps opened by spin-orbit coupling (SOC). We note here that, while only SOC is assumed to contribute to the band gaps in the previous study, our analysis demonstrates that the breathing effect can also open similar gaps [24]. Very importantly, the resulting Berry curvature should have different characteristics depending on the origins of the gaps: SOC or the breathing effect (Supplemental Material Notes 1 and 2 [25]). Based on group theory [26–28], our analysis without SOC shows two degeneracies in a bilayer at the K points, as claimed in Ref. [20]. Nevertheless, this result does not necessarily mean that the breathing effect [Supplemental Material Fig. S4(b) [25]] disappears.

We also point out that angle-resolved photoemission spectroscopy (ARPES) experiments with vacuum ultraviolet light (VUV), previously used [20], could become so surface sensitive as to capture only surface states because of the short mean free path of the photoelectrons excited [29]. The shortcoming of VUV-ARPES could be, however, solved by using soft x ray (SX) as a photon source; the mean free path becomes longer than that of VUV-ARPES, making SX-ARPES more suited to study bulk properties of a crystal [30]. In this Rapid Communication, we utilize both surface-sensitive VUV-ARPES and relatively bulk-sensitive SX-ARPES to distinguish the bulk and surface electronic structures of Fe_3Sn_2. In contrast

*kuroken224@issp.u-tokyo.ac.jp
†kondo1215@issp.u-tokyo.ac.jp

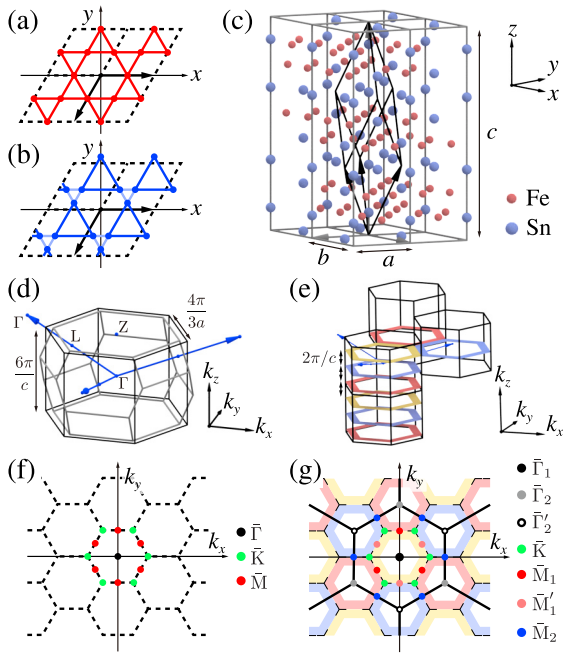

FIG. 1. Structure of kagome lattice and Fe_3Sn_2. (a), (b) Ideal and breathing kagome lattice, respectively. (c) Crystal structure of Fe_3Sn_2 with conventional unit cells (gray lines) and primitive unit cell (black lines). The lattice constants of the conventional unit cell were determined to be $a = b = 5.35$ Å and $c = 19.82$ Å by x-ray diffraction measurements. (d) Brillouin zone (gray lines), hexagonal column unit cell (black lines), and unit vectors (blue arrows). (e) Stacking of the hexagonal column unit cells. (f), (g) Periodicity for the two-dimensional structure (black dashed lines) and that for the three-dimensional one (black solid lines), respectively. High-symmetry points are marked by circles.

to VUV-ARPES, our SX-ARPES experiments reveal three-dimensional band dispersions, moderately consistent with those of Kohn-Sham orbitals in density functional theory (DFT) [31]. This coincidence suggests that the presence of Weyl semimetallic states could be the origin of the AHE.

Fe_3Sn_2 crystals were grown by the chemical vapor transport method. VUV-ARPES measurements were performed at I05 ARPES beamline of Diamond Light Source [32]. The photon energies used ranged from 50 to 120 eV, and the overall energy resolution was less than 20 meV. SX-ARPES measurements were performed at BL25SU of SPring-8 [33]. The photon energies used ranged from 380 to 620 eV, and the overall energy resolution was less than 60 meV. In both experiments, the samples were cleaved *in situ* along the (001) plane at an ultrahigh vacuum of $\sim 3 \times 10^{-8}$ Pa, and the temperature for measurements was set at about 60 K. In our DFT calculations without SOC, we used QUANTUM ESPRESSO code [34,35] and ultrasoft pseudopotentials [36,37]. Atomic positions were optimized using a $16 \times 16 \times 16$ k mesh, and then self-consistent calculations were performed with a $32 \times 32 \times 32$ k mesh. During the calculations, the size of the primitive unit cell was fixed to that experimentally determined.

The reciprocal space associated with the crystal structure needs to be carefully taken into account to understand the ARPES signature. Fe_3Sn_2 is composed of a Fe-Sn kagome bilayer and a Sn honeycomb lattice stacked along the z direction [Fig. 1(c)]. While the conventional unit cell is shaped by the quadrangular prism [gray lines in Fig. 1(c)], a smaller rhombohedral primitive unit cell is also defined (black lines). Here we consider the periodicity in the reciprocal space for the primitive unit cell, which should be observed for the bulk bands by ARPES. For ease of understanding, we use a hexagonal column [black lines in Fig. 1(d)] as a unit cell of the reciprocal space, instead of the BZ (gray lines). The hexagonal columns are simply stacked along the k_z direction, whereas the ones touched on the side surfaces are shifted by $2\pi/c$ from each other [Fig. 1(e)]. The colored hexagonal frames in Fig. 1(e) can be neglected in a two-dimensional electronic structure (or surface states), which thus expects a small hexagonal periodicity, as presented in Fig. 1(f). In contrast, the colored frame should be taken into account for a three-dimensional electronic structure (or bulk states), leading to a longer periodicity [Fig. 1(g)]. The rhombohedral unit cell, therefore, enables us to distinguish between two- and three-dimensional electronic structures not only from k_z dispersion but also from in-plane periodicity.

Here we provide a theoretical consideration of the electronic states allowed by the crystal property of Fe_3Sn_2 (see Notes 1–3 [25] for details). Assuming two-dimensionality, the nearest-neighbor tight-binding model for the breathing kagome lattice presents cone-shaped dispersions centered at the $\bar{K}$ points, which become gapped even without SOC [Ref. [24] and Fig. S1(c) [25]]. The band gap opened either by the breathing effect or SOC [Refs. [20,24], and Fig. S1(b) [25]] can generally be understood by group theory (Note 1 [25]). Significantly, the Berry curvature generated by the breathing effect [Fig. S2(b) [25]] is expressed as an odd function, whereas that by SOC [Fig. S2(c) [25]] is expressed as an even function. Hence, the values of the Berry curvature are not uniquely determined by the size of the band gap.

This argument for the two-dimensional case can be extended to that for the three-dimensional case, in which the group theoretical analysis similarly confirms that electronic states have two degeneracies in a breathing bilayer at the K points without SOC (Note 3 [25]). Importantly, this result, however, does not necessarily mean that massless Dirac fermionic states must be generated [Fig. S4(b) [25]]. Moreover, these arguments based on the conventional unit cell are not straightforward for the understanding of the physical properties of Fe_3Sn_2 such as ARPES spectra, because they have a periodicity corresponding to the primitive unit cell. Hereafter, we investigate the electronic structure observed by ARPES and discuss it based not on the conventional unit cell associated with the kagome lattice but on the rhombohedral primitive unit cell, which is the essential structure.

Figure 2(a) plots the Fermi surface map along k_x-k_y obtained by VUV-ARPES. The periodicity of ARPES intensities is found to be short, agreeing with that for surface states; while some traces of bulk states are partially obtained at particular binding energies (Note 5 [25]), these are not significant. The feature of surface states is more clearly identified in Fig. 2(b), which extracts the momentum distribution curve (MDC) across the $\bar{\Gamma}$ point [a red line in Fig. 2(a)]. Along the momentum cut, spectral peaks corresponding to k_F positions periodically appear, as confirmed by a good matching between

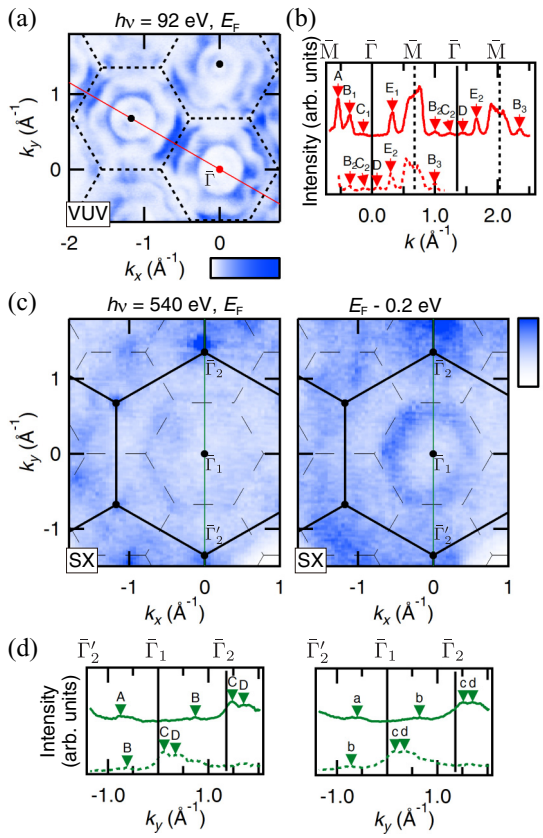

FIG. 2. Constant-energy mappings of Fe_3Sn_2. (a) Fermi surface mapping measured by VUV-ARPES. The dashed lines represent the periodicity of the two-dimensional structure. (b) Momentum distribution curve (MDC) along the red line on (a), and that shifted by one period along the momentum direction. (c) Constant-energy mappings at E_F (left panel) and $E_F - 0.2$ eV (right panel) measured by SX-ARPES. The dashed and solid lines represent the periodicities of the two- and three-dimensional structures, respectively. (d) MDCs along the green lines on (c) and those shifted by one period of the two-dimensional periodicity [dashed lines in (c)].

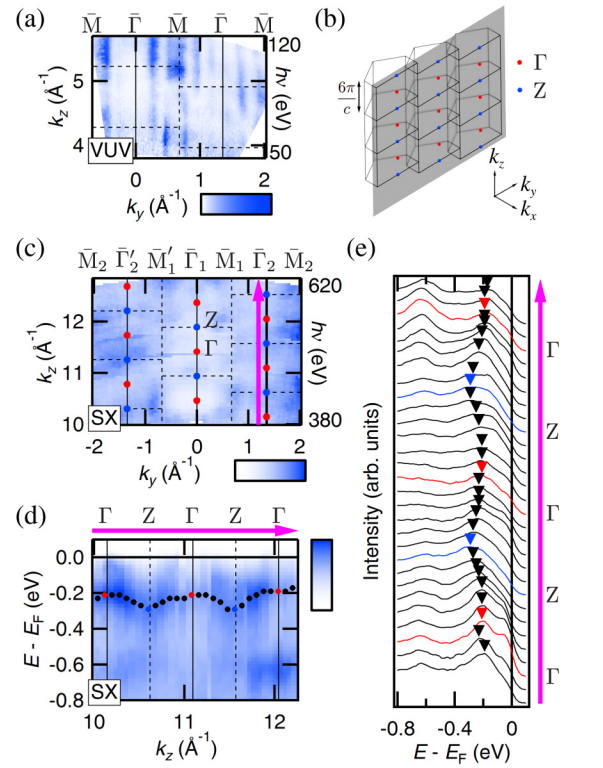

FIG. 3. k_z dispersion of electronic states in Fe_3Sn_2. (a) k_y-k_z mapping at the Fermi energy measured by VUV-ARPES. (b) Cross section at $k_x = 0$ of the stacked hexagonal unit cells. (c) The k_y-k_z mapping at $E_F - 0.4$ eV measured by SX-ARPES. (d), (e) Energy-momentum mapping along the $\bar{\Gamma}_2$ line [the pink arrow in (c)] and the corresponding energy distribution curves, respectively. For clarity, the spectra at the Γ and Z points are colored by red and blue, respectively. The spectral peaks are marked by triangles, and the corresponding energy states are plotted by circles in (d).

the original MDC and that shifted by one period (the distance between adjacent $\bar{\Gamma}$ points). In sharp contrast, the Fermi surface map by SX-ARPES [the left panel of Fig. 2(c)] exhibits a much longer periodicity: The large hexagonal pocket centered at the $\bar{\Gamma}_1$ point is different from the much smaller circular pockets at the $\bar{\Gamma}_2$ points. These features become much clearer at slightly higher binding energy ($E_F - 0.2$ eV), as demonstrated in the right panel of Fig. 2(c). The MDCs across $\bar{\Gamma}$ [green lines in Fig. 2(c)] also confirm that SX-ARPES intensities lack signatures with the two-dimensional periodicity [Fig. 2(d)], rather being compatible with bulk states with a longer periodicity.

The periodicity of the band structure is further investigated along the k_z direction by changing the photon energy ($h\nu$) in Fig. 3. For the data measured by VUV-ARPES, the k_z dispersion is almost negligible [Fig. 3(a)]; while the spectral intensities modulate with photon energy due to the matrix element effects, the peak positions of MDCs are unchanged [Fig. S7(b) [25]], indicating that these spectra have dominant contribution from the surface states. In contrast, the results of SX-ARPES display a clear k_z dispersion [Figs. 3(c)–3(e)] with the periodicity for the bulk state, which is illustrated by misaligned rectangles along k_y-k_z [Fig. 3(b)]. In Fig. 3(d), we extract the energy-momentum map along k_z across the Γ and Z points, and can indeed confirm the periodic oscillation expected for the bulk states by tracking a spectral peak position (filled circles) for each energy distribution curve [Fig. 3(e)].

To further understand the bulk band structure in Fe_3Sn_2, here we compare the ARPES results by SX-ARPES with the dispersions of Kohn-Sham orbitals in DFT along the momentum cuts represented in Fig. 4(h). The Γ point in the three-dimensional BZ can be accessed at $h\nu = 580$ eV in the SX-ARPES measurements. Figures 4(a) and 4(c) show the energy-momentum maps along the k_y and k_x directions, respectively. The curvature plot [38] of a wide-energy map clearly shows band dispersions, which are complex as seen in the DFT calculations [Fig. S8(b) [25]]. Here we focus on several bands near E_F around the Γ_1 point and obtained consistency with the DFT band dispersions, which are emphasized by thick curves. This agreement is more clearly demonstrated in Figs. 4(b) and 4(d) by extracting MDCs, in which one can trace two electron bands and one hole band centered at the Γ_1 point (see overlaid guides). Although the resolution of SX-ARPES is not perfect, this result reasonably

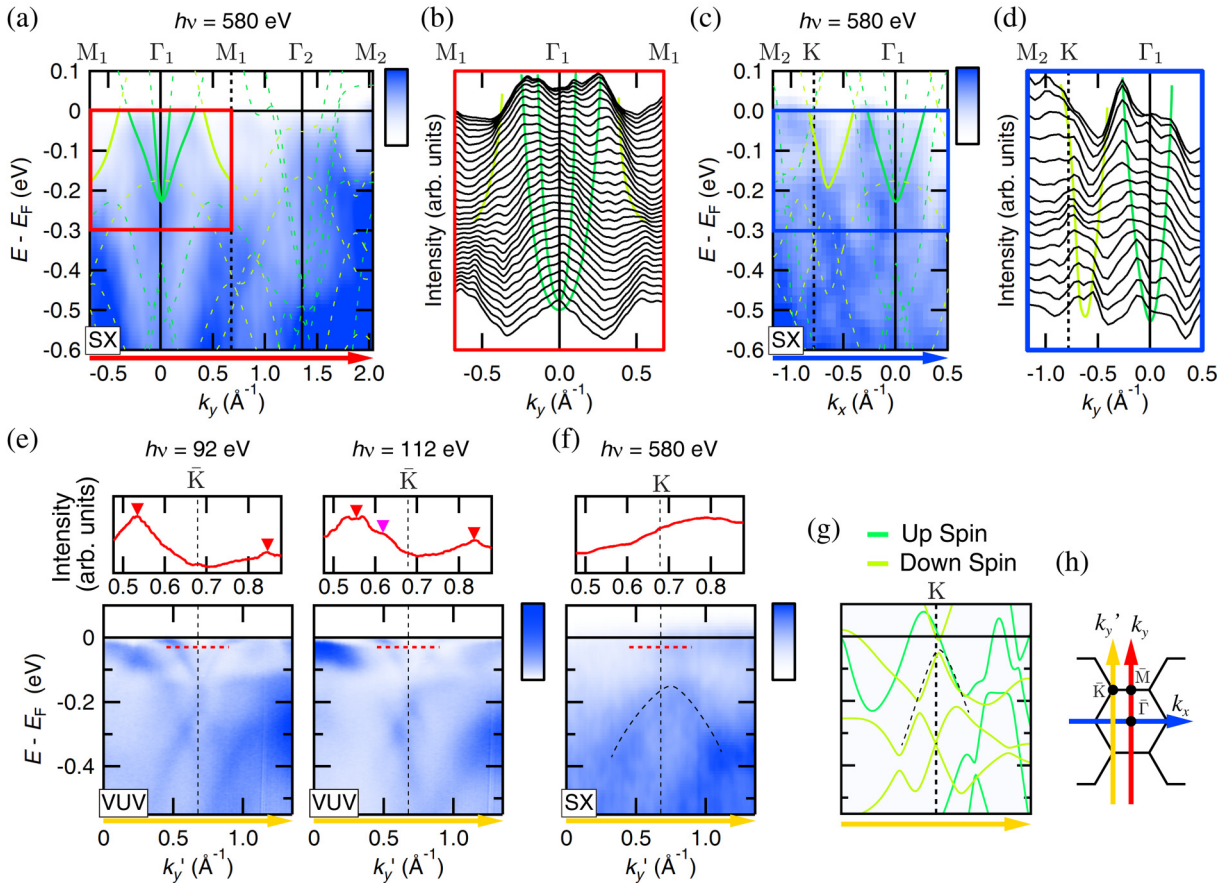

FIG. 4. Comparison between ARPES data and the dispersions of DFT calculations. (a) Energy-momentum mapping measured along the k_y direction [a red arrow in (h)]. The dispersions of the DFT calculations (green and yellow-green curves) are overlaid and those agreeing well with the ARPES results are particularly emphasized with thick curves. (b) Momentum distribution curves (MDCs) extracted from the red rectangular region in (a). Overlaid curves are guides for the eye, which correspond to the emphasized DFT dispersions. (c) Energy-momentum mapping along the k_x direction [a blue arrow in (h)], with overlaid DFT dispersions. (d) MDCs extracted from the blue rectangular region in (c), with schematic band dispersions plotted as guides for the eye. (e) Energy-momentum maps (bottom panels) obtained by VUV-ARPES along the yellow arrow in (h), exhibiting massive Dirac cones centered at the $\bar{K}$ point. In the top panels, MDCs at $E_F - 0.03$ eV (red dashed lines in the mappings) are extracted. The spectral peaks for outer and inner cones are marked by red and pink triangles, respectively. (f) SX-ARPES results of energy-momentum mapping (bottom panel) and MDC (top panel) along the same momentum cut as in (e). (g) DFT band dispersions in the same momentum cut as in (e) and (f). Cone-shaped dispersions are traced with dashed curves in (f) and (g). (h) Schematic representing the two-dimensional periodicity with momentum cuts (arrows) along which the above ARPES mappings are taken.

supports a theoretical prediction by *ab initio* calculations based on DFT that Fe_3Sn_2 is a magnetic Weyl semimetal [39].

Two massive Dirac fermionic states around the $\bar{K}$ points have been previously observed by VUV-ARPES [20], and the same results are indeed reproduced by our VUV-ARPES measurements [Fig. 4(e)]. The unique structures have been assumed to originate from bilayer stacking with weak interlayer coupling. However, we emphasize here that these features are not obtained in DFT band dispersions [Fig. 4(g)], no matter what k_z value is selected [Fig. S9 [25]]. At most, only one pair of cones is obtained in the DFT calculations, and such an electronic structure is also confirmed in our bulk-sensitive SX-ARPES data [dashed curve in Fig. 4(f)]. While the steepness of the cones in Figs. 4(f) and 4(g) seems to be different from each other, this circumstance would not be critical for our arguments since the scaling and shift of band dispersions in the energy direction often become required to get a good agreement between DFT calculations and ARPES experiments [14,16]. Most importantly, the fact that two Dirac states with negligible k_z dispersions are observed only by VUV-ARPES [Fig. 4(e)] leads us to conclude that these dispersions are derived dominantly from the surface states, which are unlikely related to bulk phenomena such as the AHE.

In conclusion, we combined two experimental techniques of surface-sensitive VUV-ARPES and relatively bulk-sensitive SX-ARPES, and separately observed two-dimensional states on the surface and three-dimensional states in the bulk of the kagome bilayer crystal Fe_3Sn_2. The crystal structure with the rhombohedral primitive unit cell allowed us to separate two- and three-dimensional states by observing the periodicity of ARPES intensities on a plane parallel to the k_x-k_y plane as well as in the k_z dispersion. We reveal that the massive Dirac fermionic states, which have been suggested to be the origin of the AHE, have dominant contribution from the surface states. In addition, we argue the requirement of taking

into account the breathing effect on the degeneration property and the Berry curvature (Notes 1–3 [25]) in the physics of the kagome lattice. Moreover, the rhombohedral unit cell of Fe_3Sn_2 and the observed three-dimensional electronic structure make it not straightforward to discuss the properties of this material based on the two-dimensional kagome physics. One possible explanation for the large AHE is that Fe_3Sn_2 is a magnetic Weyl semimetal. A good agreement between bulk states observed by SX-ARPES and band dispersions obtained by DFT calculations supports this perspective.

We thank Y. Ishida for supporting the analysis of our ARPES data [40]. This work is also supported by Grants-in-Aid for Scientific Research (B) (Grants No. 18H01165 and No. 19H02683) and Photon and Quantum Basic Research Coordinated Development Program from MEXT. The SX synchrotron radiation experiments were performed with the approval of JASRI (Proposals No. 2019A1087 and No. 2019B1092). We thank Diamond Light Source for access to beamline I05 (SI24488-1) that contributed to the results presented here.

[1] N. Ashcroft and N. Mermin, *Solid State Physics*, HRW international editions (Holt, Rinehart and Winston, New York, 1976).
[2] M. V. Berry, Proc. R. Soc. London, Ser. A **392**, 45 (1984).
[3] D. J. Thouless, M. Kohmoto, M. P. Nightingale, and M. den Nijs, Phys. Rev. Lett. **49**, 405 (1982).
[4] M. Z. Hasan and C. L. Kane, Rev. Mod. Phys. **82**, 3045 (2010).
[5] C. L. Kane and E. J. Mele, Phys. Rev. Lett. **95**, 226801 (2005).
[6] G. Xu, H. Weng, Z. Wang, X. Dai, and Z. Fang, Phys. Rev. Lett. **107**, 186806 (2011).
[7] S. M. Huang, S. Y. Xu, I. Belopolski, C. C. Lee, G. Chang, B. Wang, N. Alidoust, G. Bian, M. Neupane, C. Zhang, S. Jia, A. Bansil, H. Lin, and M. Z. Hasan, Nat. Commun. **6**, 7373 (2015).
[8] A. A. Soluyanov, D. Gresch, Z. Wang, Q. Wu, M. Troyer, X. Dai, and B. A. Bernevig, Nature (London) **527**, 495 (2015).
[9] G. Autès, D. Gresch, M. Troyer, A. A. Soluyanov, and O. V. Yazyev, Phys. Rev. Lett. **117**, 066402 (2016).
[10] H. Yang, Y. Sun, Y. Zhang, W.-J. Shi, S. S. P. Parkin, and B. Yan, New J. Phys. **19**, 015008 (2017).
[11] S.-Y. Xu *et al.*, Science **349**, 613 (2015).
[12] B. Q. Lv, H. M. Weng, B. B. Fu, X. P. Wang, H. Miao, J. Ma, P. Richard, X. C. Huang, L. X. Zhao, G. F. Chen, Z. Fang, X. Dai, T. Qian, and H. Ding, Phys. Rev. X **5**, 031013 (2015).
[13] B. Q. Lv, N. Xu, H. M. Weng, J. Z. Ma, P. Richard, X. C. Huang, L. X. Zhao, G. F. Chen, C. E. Matt, F. Bisti, V. N. Strocov, J. Mesot, Z. Fang, X. Dai, T. Qian, M. Shi, and H. Ding, Nat. Phys. **11**, 724 (2015).
[14] K. Kuroda *et al.*, Nat. Mater. **16**, 1090 (2017).
[15] M.-Y. Yao, N. Xu, Q. S. Wu, G. Autès, N. Kumar, V. N. Strocov, N. C. Plumb, M. Radovic, O. V. Yazyev, C. Felser, J. Mesot, and M. Shi, Phys. Rev. Lett. **122**, 176402 (2019).
[16] D. F. Liu, A. J. Liang, E. K. Liu, Q. N. Xu, Y. W. Li, C. Chen, D. Pei, W. J. Shi, S. K. Mo, P. Dudin, T. Kim, C. Cacho, G. Li, Y. Sun, L. X. Yang, Z. K. Liu, S. S. P. Parkin, C. Felser, and Y. L. Chen, Science **365**, 1282 (2019).
[17] J. C. Slonczewski and P. R. Weiss, Phys. Rev. **109**, 272 (1958).
[18] H.-M. Guo and M. Franz, Phys. Rev. B **80**, 113102 (2009).
[19] Q. Wang, S. Sun, X. Zhang, F. Pang, and H. Lei, Phys. Rev. B **94**, 075135 (2016).
[20] L. Ye, M. Kang, J. Liu, F. von Cube, C. R. Wicker, T. Suzuki, C. Jozwiak, A. Bostwick, E. Rotenberg, D. C. Bell, L. Fu, R. Comin, and J. G. Checkelsky, Nature (London) **555**, 638 (2018).
[21] H. Li, B. Ding, J. Chen, Z. Li, Z. Hou, E. Liu, H. Zhang, X. Xi, G. Wu, and W. Wang, Appl. Phys. Lett. **114**, 192408 (2019).
[22] J. X. Yin *et al.*, Nature (London) **562**, 91 (2018).
[23] Z. Lin, J.-H. Choi, Q. Zhang, W. Qin, S. Yi, P. Wang, L. Li, Y. Wang, H. Zhang, Z. Sun, L. Wei, S. Zhang, T. Guo, Q. Lu, J.-H. Cho, C. Zeng, and Z. Zhang, Phys. Rev. Lett. **121**, 096401 (2018).
[24] A. Bolens and N. Nagaosa, Phys. Rev. B **99**, 165141 (2019).
[25] See Supplemental Material at http://link.aps.org/supplemental/10.1103/PhysRevB.101.161114 for calculations of band dispersions and the Berry curvatures, group-theoretical analysis, and additional data of ARPES experiments and DFT calculations.
[26] L. P. Bouckaert, R. Smoluchowski, and E. Wigner, Phys. Rev. **50**, 58 (1936).
[27] R. J. Elliott, Phys. Rev. **96**, 280 (1954).
[28] W. Opechowski, Physica **7**, 552 (1940).
[29] C. Powell, A. Jablonski, I. Tilinin, S. Tanuma, and D. Penn, J. Electron Spectrosc. Relat. Phenom. **98-99**, 1 (1999).
[30] V. Strocov, L. Lev, M. Kobayashi, C. Cancellieri, M.-A. Husanu, A. Chikina, N. Schröter, X. Wang, J. Krieger, and Z. Salman, J. Electron Spectrosc. Relat. Phenom. **236**, 1 (2019).
[31] W. Kohn, Rev. Mod. Phys. **71**, 1253 (1999).
[32] M. Hoesch, T. K. Kim, P. Dudin, H. Wang, S. Scott, P. Harris, S. Patel, M. Matthews, D. Hawkins, S. G. Alcock, T. Richter, J. J. Mudd, M. Basham, L. Pratt, P. Leicester, E. C. Longhi, A. Tamai, and F. Baumberger, Rev. Sci. Instrum. **88**, 013106 (2017).
[33] Y. Senba *et al.*, AIP Conf. Proc. **1741**, 030044 (2016).
[34] P. Giannozzi *et al.*, J. Phys.: Condens. Matter **21**, 395502 (2009).
[35] P. Giannozzi *et al.*, J. Phys.: Condens. Matter **29**, 465901 (2017).
[36] A. M. Rappe, K. M. Rabe, E. Kaxiras, and J. D. Joannopoulos, Phys. Rev. B **41**, 1227 (1990).
[37] We used the pseudopotentials Fe.pbe-n-rrkjus_psl.1.0.0.UPF and Sn.pbe-dn-rrkjus_psl.1.0.0.UPF from the QUANTUM ESPRESSO pseudopotential data base, http://www.quantum-espresso.org/pseudopotentials.
[38] P. Zhang, P. Richard, T. Qian, Y.-M. Xu, X. Dai, and H. Ding, Rev. Sci. Instrum. **82**, 043712 (2011).
[39] M. Yao, H. Lee, N. Xu, Y. Wang, J. Ma, O. V. Yazyev, Y. Xiong, M. Shi, G. Aeppli, and Y. Soh, Switchable Weyl nodes in topological Kagome ferromagnet Fe_3Sn_2, arXiv:1810.01514.
[40] Y. Ishida and S. Shin, Rev. Sci. Instrum. **89**, 043903 (2018).